

DMSP Poynting Flux: Data Processing and Inter-spacecraft Comparisons

Liam Kilcommons¹, Delores J. Knipp¹, Marc R. Hairston², and W. Robin Coley²

¹University of Colorado Boulder

²University of Texas at Dallas

November 22, 2022

Abstract

Poynting flux calculated from LEO spacecraft in-situ ion drift and magnetic field measurements is an important measure of energy exchange between the magnetosphere and ionosphere. Defense Meteorological Satellite Program (DMSP) spacecraft provide an extensive back-catalog of ion drift and magnetic perturbation measurements, from which quasi-steady Poynting flux could be calculated. However, since DMSP are operations-focused spacecraft, data must be carefully preprocessed for research use. We describe an automated approach for calculating earthward Poynting flux focusing on pre-processing and quality control. We produce a Poynting flux dataset using 9 satellite-years of DMSP F15, F16 and F18 observations. To validate our process we inter-compare Poynting flux from different spacecraft using more than 2000 magnetic conjunction events. We find no serious systematic differences. We further describe and apply an equal-area binning technique to obtain average spatial patterns of Poynting flux, magnetic perturbation, electric field and ion drift velocity. We perform our analysis using all components of electric and magnetic field and comment on the adverse consequences of the typical single-electric-field-component DMSP Poynting flux approximation on inter-spacecraft agreement. Including full-field components significantly increases the relative strength of near-cusp Poynting flux and increases the integrated high-latitude Poynting flux by ~25%

DMSP Poynting Flux: Data Processing and Inter-spacecraft Comparisons

Liam M. Kilcommons¹, Delores J. Knipp¹, Marc Hairston², W. Robin Coley²

¹Ann and H.J. Smead Aerospace Engineering Sciences, University of Colorado, Boulder

²William B. Hanson Center for Space Sciences, University of Texas, Dallas

Key Points:

- We describe the data processing for a new Poynting flux (PF) database and provide code access
- We provide an inter-comparison of PF from 3 DMSP Spacecraft via a conjunction analysis
- Use of all electric field components to calculate PF significantly improves the inter-comparison

Corresponding author: Liam M. Kilcommons, liam.kilcommons@colorado.edu

Abstract

Poynting flux calculated from LEO spacecraft in-situ ion drift and magnetic field measurements is an important measure of energy exchange between the magnetosphere and ionosphere. Defense Meteorological Satellite Program (DMSP) spacecraft provide an extensive back-catalog of ion drift and magnetic perturbation measurements, from which quasi-steady Poynting flux could be calculated. However, since DMSP are operations-focused spacecraft, data must be carefully preprocessed for research use. We describe an automated approach for calculating earthward Poynting flux focusing on pre-processing and quality control. We produce a Poynting flux dataset using 9 satellite-years of DMSP F15, F16 and F18 observations. To validate our process we inter-compare Poynting flux from different spacecraft using more than 2000 magnetic conjunction events. We find no serious systematic differences. We further describe and apply an equal-area binning technique to obtain average spatial patterns of Poynting flux, magnetic perturbation, electric field and ion drift velocity. We perform our analysis using all components of electric and magnetic field and comment on the adverse consequences of the typical single-electric-field-component DMSP Poynting flux approximation on inter-spacecraft agreement. Including full-field components significantly increases the relative strength of near-cusp Poynting flux and increases the integrated high-latitude Poynting flux by $\sim 25\%$.

Plain Language Summary

We describe processing of observations from approximately 45000 Defense Meteorological Satellite Program (DMSP) spacecraft orbits over the course of three years, which can be used to study the climatology of electromagnetic energy transfer (also known as Poynting flux) between the magnetosphere and ionosphere. Observations from three instruments on three operational spacecraft are used to produce the necessary estimates of electric field and magnetic field perturbations that go into the Poynting flux calculation. Our processing pipeline includes data checking, baseline removal and spatial binning of electric and magnetic field perturbations to produce maps of the individual elements of Poynting flux. We bin the results in equal-area bins for each hemisphere. To verify our work, we provide comparisons of individual measurements made by different spacecraft when they are close to each other in space and time. In general we find the best agreement when we use all components of available field data. Including full-field components significantly increases the relative strength of near-cusp Poynting flux and increases the integrated high-latitude Poynting flux by $\sim 25\%$.

1 Introduction

Episodic orbit-perturbing events of the early space age (e.g. February 1958, July 1959 and November 1960) produced several lines of inquiry about their root causes. Jacchia (1959a) and Jacchia (1959b) first proposed variations in solar shortwave energy and then ‘corpuscular’ deposition associated with magnetic storms as sources, while Dessler (1959) advocated for hydromagnetic wave heating. Availability of early solar wind data led Cole (1966) to assert that variation in storm-time energy deposition in the thermosphere arising from solar wind magnetosphere interactions was the likely dominant source of episodic low Earth orbit (LEO) perturbations and enhanced satellite drag. An early NASA mission, Injun-5/Explorer-40, indicated that very low frequency electromagnetic energy transfer was predominantly earthward at plasmaspheric altitudes (Mosier & Gurnett, 1969). Quantifying the electromagnetic energy transfer (now often referred to as ‘Poynting flux’) between the magnetosphere and ionosphere has been challenging during the last half century due to the need for *in situ* coincident measurement of magnetic and electric fields and their variation. We discuss the data processing required to take advantage of the Defense Meteorological Satellite Program (DMSP) coincident measurements of ion drift and magnetic field to calculate quasi-steady Poynting flux (PF).

63 Estimates of Alfvénic (wave) and quasi-steady Poynting flux have been produced
 64 from LEO and beyond starting in the late 1960s. Recently Kaeppler et al. (2022) reviewed
 65 the Poynting flux literature and provided summaries of mission results from dozens of
 66 studies. Their Table 1 shows reported typical quasi-steady Poynting flux values of 1–
 67 $10\text{mW}/\text{m}^2$ near the dayside cusp and auroral zones of both hemispheres (mapped to ap-
 68 proximately 100 km). Originally the maps of quasi-steady Poynting flux were rather coarse
 69 with only enough data for averaging over both hemispheres (Gary et al., 1995) and (Olsson
 70 et al., 2004). Both of these studies showed the intensity and areal coverage of Poynting
 71 flux deposition increased with increasing geomagnetic activity. Empirical, combined-hemisphere
 72 models of quasi-steady Poynting flux have been developed (e.g., (Cosgrove et al., 2014);(Weimer,
 73 2005)) and binned by the interplanetary magnetic field (IMF) and solar wind conditions.

74 During the last decade a growing archive of DMSP data has supported investiga-
 75 tion of intense Poynting flux deposition into both hemispheres. Huang et al. (2017) found
 76 values of Poynting flux exceeding $100\text{mW}/\text{m}^2$ in the dawn regions of both hemispheres
 77 during a few of the main phases of the 30 geomagnetic storms they studied, however most
 78 high-latitude storm time values were less than $20\text{mW}/\text{m}^2$. D. Knipp et al. (2011) reported
 79 similar large values in the near-cusp region of both hemispheres during intervals when
 80 the IMF By component was large. Some of these studies used only the cross-track ion
 81 drift to compute the electric field contributing to Poynting flux due to concerns about
 82 the quality of the along-track ion drift data.

83 Improvements in DMSP data processing allowed D. Knipp et al. (2021) to provide
 84 quasi-steady Poynting flux maps at 220 km resolution for both hemispheres using all
 85 electric field components. As in earlier studies they showed intensity and areal coverage
 86 of Poynting flux deposition scaled with increasing activity. They also showed that, con-
 87 sistent with previous reports by Pakhotin et al. (2021) for Alfvénic Poynting flux, there
 88 is a clear preference for excess northern hemisphere deposition of Poynting flux. The present
 89 paper provides more detail about the processing and inter-comparison of spacecraft data
 90 that support the multi-year analysis in D. Knipp et al. (2021) and will support future
 91 research. We provide links to the raw data, the reduced data and supporting software.
 92 In section 2 we discuss data quality flags and binning methods as well as ion-drift base-
 93 line removal. In section 3 we demonstrate good agreement of the derived Poynting flux
 94 between spacecraft during magnetic conjunction events. We also quantify the improve-
 95 ment in Poynting flux obtained by using full-component electric field data. We conclude
 96 in section 4.

97 2 Methods and Data

98 D. Knipp et al. (2021) provided independent maps of quasi-static Poynting flux in
 99 each hemisphere based on nine-satellite years of DMSP data. The detailed creation of
 100 the dataset used in that publication will be described herein. Spatial binning was ex-
 101 ecuted to conserve spatial resolution at lower latitudes by using bins of 2 degrees lati-
 102 tude on a side (220 km) and a width in Magnetic Local Time (MLT) that produces a
 103 square-surface area for each bin. Each hemisphere has 1151 equal-area bins. To aid fu-
 104 ture researchers in understanding or reproducing our results, we use only publicly avail-
 105 able data, and make our software available via Github.

106 2.1 Data

107 The DMSP datasets are the Level-2 special sensor magnetometer (SSM) magne-
 108 tometer dataset described in L. M. Kilcommons et al. (2017) and the special sensor for
 109 ions electrons and scintillations 3 (SSIES3) ion drift and plasma parameters dataset and
 110 the SSIES2 dataset. Temporal coverage for the project is shown in Table 1. The F15 SSIES2
 111 data from Madrigal was accessed via Pysat (R. A. Stoneback et al., 2018).

Table 1. Data sources for raw data, 'Madrigal' refers to the CEDAR Madrigal database, and 'CDAWeb' refers to NASA Coordinated Data Analysis Web

Spacecraft	Years	SSIES	SSM
F15	2011-2013	Madrigal	CDAWeb
F16	2012-2014	CDAWeb	CDAWeb
F18	2012-2014	CDAWeb	CDAWeb

112

2.2 Ephemeris

113

114

115

116

117

118

119

The accuracy of spacecraft locations provided for DMSP spacecraft differs depending on the data source. For this study, we use the reprocessed spacecraft positions extracted from the DMSP magnetometer data files, as described in L. M. Kilcommons et al. (2017). These ephemeris are derived from those distributed by the NASA Satellite Situation Center Web (SSCWeb) spacecraft locator service. All magnetic coordinates reported herein are Modified Magnetic Apex (Emmert et al., 2010; van der Meeren et al., 2021) locations using a reference altitude of 110 kilometers.

120

2.3 Software and Data Processing Pipeline

121

122

123

124

125

126

127

128

129

The data processing pipeline was written in Python under Git version control using best practices such as unit testing, PEP8 style, logging, and configuration files. The purpose of the pipeline is to produce two types of data. First, we have produced orbit-by-orbit NASA Common Data Format (CDF) files which contains all of the parameters required to calculate Poynting flux. Second, by applying our equal-area binning approach, we have produced a binned data product in Hierarchical Data Format Version 5 (HDF5) format. The orbit-by-orbit files represent vectors (fields, ion drift) and Poynting flux in spacecraft frame, whereas the binned data products use magnetic coordinates (see section 2.5).

130

2.3.1 Orbit-by-Orbit Data

131

132

133

134

135

These files are created by first reading SSIES data from various source formats. Then the baseline correction for the ion drift measurements is performed. Then, the appropriate SSM data is added aligning the timestamps to produce a merged NASA Common Data Format (CDF) data file. Finally, electric field and Poynting flux are calculated. Each such file covers one full DMSP orbit for one spacecraft.

136

2.3.2 Binned Data

137

138

139

140

141

142

143

144

This process begins by reading each CDF output file, calculating field-aligned Poynting flux (and other electrodynamic parameters) and organizing the data into bins in magnetic coordinates. The result is a single Hierarchical Data Format (HDF5) output file organizing all individual Poynting flux data points by bin. We provide the software which defines the equal-area bins and the HDF5 file format as an open-source Python library called esabin (see section 5.2). The data products produced by this workflow (as used in this study and in D. Knipp et al. (2021)) have been published on Zenodo (see section 5.1).

145

2.4 Magnetometer Data

146

147

The DMSP SSM measures the three orthogonal components of the magnetic field at the spacecraft and reports average values at 1 s cadence. Post-processing corrects and/or

148 verifies the location of the spacecraft based on ground-tracking information and then cal-
 149 culates the appropriate International Geomagnetic Reference Field, \mathbf{B}_0 and removes it
 150 to yield the perturbation field, $\delta\mathbf{B}_M$. A further baseline correction intended to remove
 151 instrument artifacts and low-latitude perturbations correlated with the ring current is
 152 performed (Rich et al., 2007). This baseline signal for each $\delta\mathbf{B}$ component is found by
 153 first dividing measurements acquired during each half orbit into three segments: the first
 154 two extend from the equator to the low-latitude auroral boundaries on the evening and
 155 morning sides while the remaining segment encompasses the aurora and polar cap where
 156 most magnetic perturbations are found.

157 Auroral and polar cap boundaries are identified via automated inspection of vari-
 158 ations of precipitating particle fluxes detected by the DMSP particles sensor. Then least-
 159 squares polynomial fits are applied to each of the components of $\delta\mathbf{B}$ using the data from
 160 the subauroral segments. Baseline values of the three components are then extended via
 161 calculated polynomials across high-latitude segments to obtain \mathbf{B}_{Fit} from equator to equa-
 162 tor along entire half orbits. The corrected magnetic perturbation vectors used in this study
 163 are then calculated as $\delta\mathbf{B}_C = \delta\mathbf{B}_M - \mathbf{B}_{Fit}$. This process is described in detail in L. M. Kil-
 164 commons et al. (2017).

165 2.5 Coordinate Frames for Vector Quantities

166 It is important to note that the naming convention for directions in the spacecraft
 167 body-fixed coordinate frame used for DMSP SSM differs from that used for SSIES. For
 168 SSM the convention is \hat{x}_m is geodetic downward (nadir), \hat{y}_m perpendicular to \hat{x}_m in the
 169 plane of the spacecraft velocity vector, and \hat{z}_m completes the right-handed frame. For
 170 SSIES, \hat{x} is parallel to the spacecraft velocity vector, \hat{z} is geodetic upward (zenith), and
 171 \hat{y} completes the right-handed frame. In all calculations that follow we use the latter (SSIES)
 172 convention. In the case of vector quantities in magnetic coordinates, Modified Magnetic
 173 Apex unit vectors are used as suggested in as in Laundal and Richmond (2017). That
 174 is, we use the d basis for field measurements and the e basis for ion drift velocity.

175 2.6 Processing for Ion Drift Data

176 Automated quality control is essential in a reproducible data processing scheme.
 177 Previous work by L. M. Kilcommons et al. (2017), summarized above automated qual-
 178 ity control for the SSM magnetometer. In this work, we introduce an automated qual-
 179 ity control procedure for the SSIES ion drift.

180 2.6.1 Quality Flags

181 Several variants of SSIES data are available in public archives. The SSIES data prod-
 182 ucts used here include University of Texas Dallas (UTD) quality flags as described in Hairston
 183 and Coley (2019). The UTD quality flags are integer values which accompany each ion
 184 drift datapoint. Quality "1" data is usable, and quality "2" data may also be usable. Larger
 185 quality flag values' meanings are detailed in guide referenced above. The quality flags
 186 are assigned independently to each of the two sensors which measure ion drift. The ion
 187 drift meter (IDM) measures in the vertical (zenith) and cross-track (perpendicular to zenith
 188 and spacecraft velocity vector) directions. The retarding potential analyzer (RPA) mea-
 189 sures in the ram direction (parallel to the spacecraft velocity vector). The quality flags
 190 are calculated using in-situ-sensed or derived plasma parameters using IDM, RPA and
 191 other sensors in the SSIES instrument package.

192 In general our processing uses only quality "1" data. There is one exception to this
 193 requirement; the quality flags for version 2 SSIES (on the F15 spacecraft) are more con-
 194 servative, only producing RPA quality "1" for a few points each orbit. Therefore we in-
 195 clude quality "2" for version 2 of the SSIES (F15). Since no quality flagging algorithm

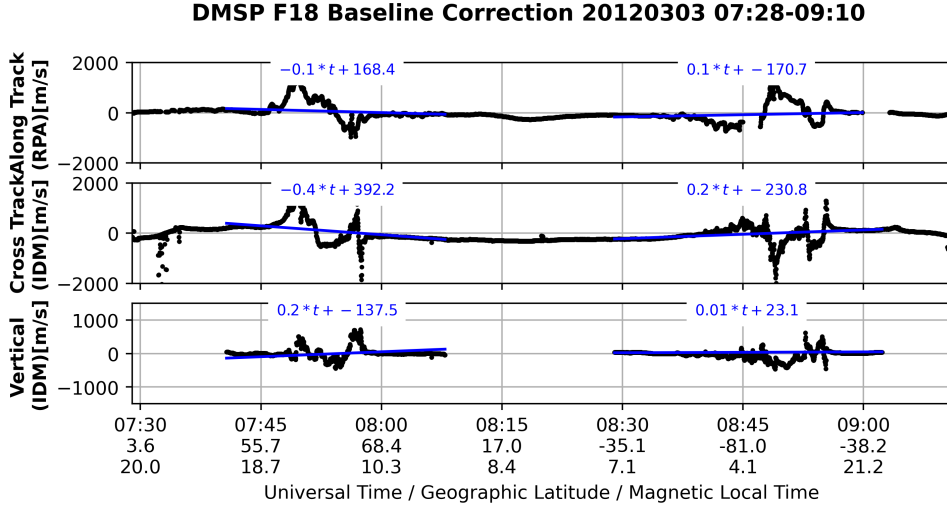


Figure 1. Example baseline correction for one full orbit (two passes) of F18 on March 3, 2012. Black curves are ion drift velocity, the baseline fits are shown in blue

196 can get every possible bad data point, we entirely discard any pass which has less than
 197 40 percent quality 1 data for IDM or less than 30 percent quality 1 data for RPA.

198 *2.6.2 Baseline*

199 Another aspect of the SSIES ion drift data which is not addressed by the quality
 200 flags is a slow variation in the total value of the RPA and IDM drifts, such that the plasma
 201 drifts that change on the order of tens-to-hundreds of kilometers appear to overlay a smoother
 202 trend which varies on the order of a quarter-to-half orbit. We will call the smoother trend
 203 the baseline. The baseline is not the co-rotation drift, as the ion drift variables in the
 204 SSIES data files mentioned in Table 1 already include this correction. Typically the base-
 205 line is treated by supposing that the drift should be near zero at mid-to-low latitude and
 206 shifting the data for each half-polar-orbit (from equator across pole to equator).

207 Our baseline approach is modeled after this typical method. We characterized the
 208 baseline on a 'pass-by-pass' basis considering only the data poleward of 40 degrees mag-
 209 netic latitude (MLAT). In this context a 'pass' is half of one orbit (the data from one
 210 orbit, for either the northern or southern hemisphere). We model the baseline as a simple
 211 line ($y = a*t + b$), with time since the spacecraft crossed 40 degrees MLAT travel-
 212 ing toward the pole as the t coordinate, and ion drift as the y coordinate. We use weighted
 213 least-squares to determine the coefficients, with weights:

$$w(t) = \frac{1}{Q(t)^2} \frac{90 - |\lambda_m(t)|}{40} \quad (1)$$

214 with $Q(t)$ as the quality of each ion drift data data point, and $\lambda_m(t)$ as the mag-
 215 netic latitude of the spacecraft. The rationale is to minimize the influence of poor qual-
 216 ity drift data (leftmost ratio) and of higher latitude ionospheric drifts (rightmost) on the
 217 baseline.

218 **2.7 Electric Field Calculation**

219 Electric field is calculated using the magnetic field measurements from SSM, and
 220 the ion drift measurements from SSIES as shown in equation 2.

$$\vec{E} = -v_{ions}\vec{\tau} \times \vec{B} \quad (2)$$

221 The components of this equation expand as:

$$E_x = v_z B_y - v_y B_z \quad (3)$$

$$E_y = v_x B_z - v_z B_x \quad (4)$$

$$E_z = v_y B_x - v_x B_y \quad (5)$$

222 Since the ram (v_x) and cross-track (v_y, v_z) drift velocities are measured by differ-
 223 ent instruments, we only calculate electric field when both instruments' data are both
 224 available and are of acceptable quality. Also it is important to note that $B_z \gg B_x, B_y$
 225 for polar regions because the geomagnetic field is nearly aligned with geodetic vertical.

226 **2.8 Poynting Flux Calculation**

227 We begin by calculating the perturbation Poynting vector (in spacecraft frame) us-
 228 ing the magnetic perturbation defined in Section 2.4:

$$\vec{S} = -\frac{1}{\mu_0} \vec{E} \times \delta\vec{B} \quad (6)$$

229 Where μ_0 is the permeability of free space.

230 Poynting flux is typically defined as the component of the Poynting vector paral-
 231 lel to the geomagnetic main field. This is often approximated as the Poynting flux in the
 232 vertical (or radial) direction:

$$S_z = \vec{S} \cdot \hat{z} \quad (7)$$

233 Where \hat{z} is a unit vector in the geodetic upward (zenith) direction.

234 We do not use this approximation, and instead follow Olsson et al. (2004) and com-
 235 pute the field-aligned Poynting flux into the ionosphere, scaling to an altitude of 110 km:

$$S_B = \frac{|\vec{B}_{110}|}{|\vec{B}_0|} \frac{(\vec{B}_{110} \cdot \hat{z})}{|\vec{B}_{110}|} (\mp \hat{b}_0 \cdot \vec{S}) \quad (8)$$

236 Where \vec{B}_0 is the International Geomagnetic Reference Frame (IGRF) at spacecraft
 237 location, \hat{b}_0 is a unit vector in the direction of \vec{B}_0 , \vec{B}_{110} is \vec{B}_0 at an altitude of 110 kilo-
 238 meters. The sign in front of \hat{b}_0 ensures the flux is directed into the ionosphere in both
 239 northern (negative) and southern (positive) hemispheres. Note that the term ($\cos I =$
 240 $\frac{(\vec{B}_{110} \cdot \hat{z})}{|\vec{B}_{110}|}$) is nearly unity (ranging from 0.94 to 1.00) for mid-to-high magnetic latitudes
 241 ($|\lambda_m| > 60$).

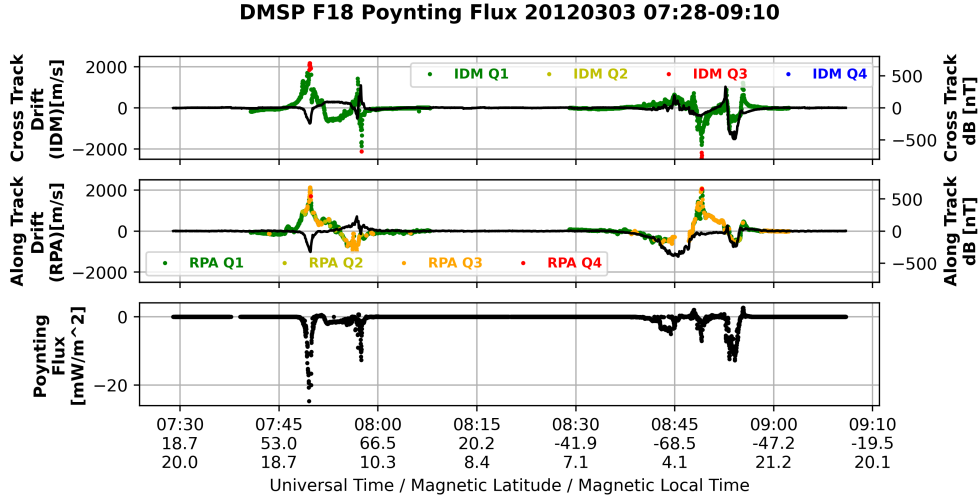


Figure 2. Example Poynting flux calculated for one full orbit (two passes) of F18 on March 3, 2012. Ion drift is shown colored by associated quality flag with green indicating good quality. Magnetic perturbations are shown in black. Poynting flux was calculated using only high quality (green) ion drift

242

2.9 Spatial Binning and Statistics

243

244

245

246

247

248

249

250

Many studies calculating Poynting flux from in-situ electromagnetic measurements have used spatial binning in magnetic coordinates to understand where and under what conditions strong Poynting flux occurs. Most authors use magnetic latitude and magnetic local time (MLT) to define their bins. For instance, all bins might be 3 degrees in latitude by 1 hour magnetic local time. However, considered as sections of the surface of a sphere, constant latitude/MLT bins produce severely biased sampling: the area of a bin at mid-latitudes is an order of magnitude greater than the area of a bin near the pole.

251

252

253

254

255

256

We use an alternative approach, in which bins have a constant latitude width, but the width in MLT varies with latitude to approximate equal surface area for each bin. The top row of 3 shows binned data from passes in the northern and southern hemisphere. This approach introduces complications for how the data is stored. For reproducibility, our open-source software package (esabin) which implements both this approach and the constant MLT approach above is available on Github.

257

2.9.1 Binning Procedure

258

259

260

261

Another practical consideration for this study was how to store and retrieve the binned data. The amount of data from multiple spacecraft years of high-cadence (F15: 4-second sampling, F16 and F18: 1-second sampling) data is very large and cannot be stored easily in memory (RAM) on a typical desktop computer.

262

263

264

265

266

267

We devised a two step solution to this problem. The first step is to reorganize the data into individual crossings of particular bins, and store this new dataset in a file, instead of in RAM. This new dataset is a Hierarchical Data Format (HDF) file with a Group for each bin. The HDF format allows data to be written to any Group at any time, so it becomes feasible to store the entire multi-year, multi-spacecraft dataset in one file by adding the data one orbit at a time. The result is that each bin's Group is filled with

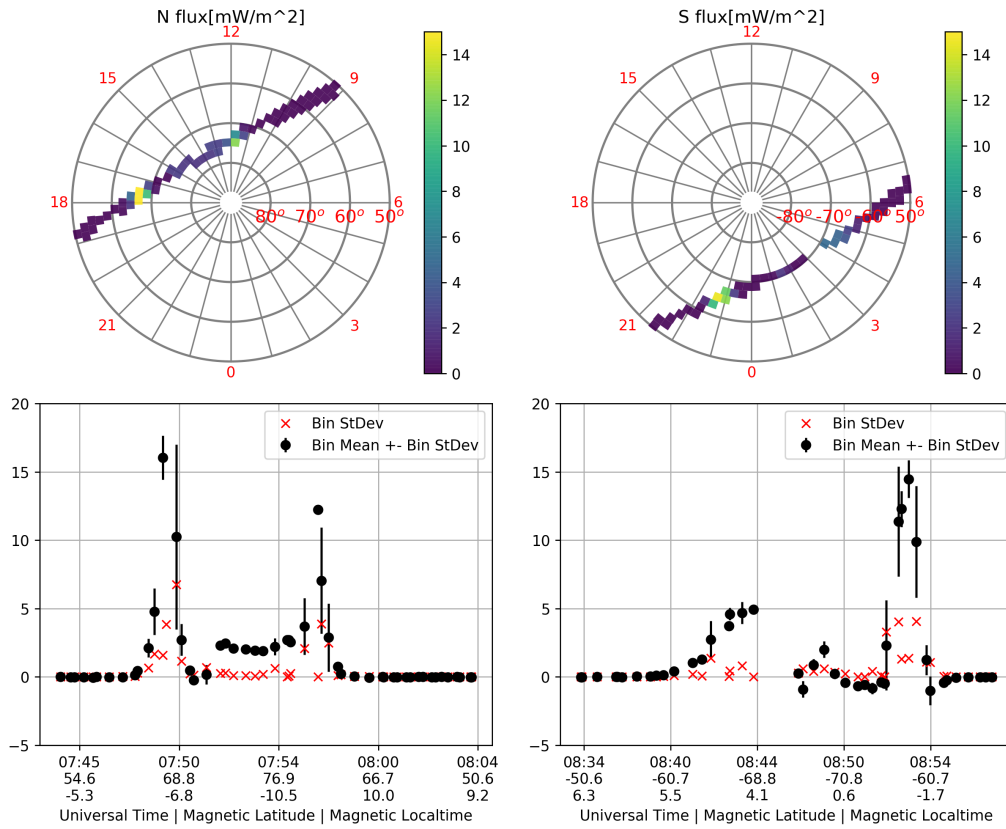


Figure 3. Binned and reduced Poynting flux for previously shown orbit of F18 on March 3, 2012. Northern hemisphere PF is in the left column while southern hemisphere PF is in the right column. Color in polar plots indicates downward Poynting flux magnitude, matching black curve in line plots. Error bars and red 'x' markers in line plots represent sub-bin-scale variability as quantified by the standard deviation of 1-second measurements in bin. Missing dawn-sector bins in top right due to localized quality drop in ion drift measurements

268 Datasets, each representing one spacecraft crossing that bin at one specific time. Each
 269 such Dataset contains around 15 samples of 1 second-data, or around 4 samples of 4-second
 270 data. Also each Dataset stores additional metadata, most importantly the date and time
 271 of the crossing and the 'F-number' of the spacecraft (e.g. F15). The resulting file is very
 272 large and preserves every data point of the original data.

273 The second step is to further reduce the data size by considering each bin cross-
 274 ing (each Dataset in the HDF file) as one 'sample' of the spatial area of that bin and stor-
 275 ing only the mean and standard deviation of the data from that bin crossing. In addi-
 276 tion to making the data smaller, this also 'standardizes' the data (for instance, remov-
 277 ing any need to take the 4-second versus 1-second sampling into account).

278 After the two-step reduction process, the data from each bin is much more easily
 279 manipulated. For instance the average of the reduced data, for each bin, for several elec-
 280 trodynamic parameters is shown in figure 4. For vector quantities, separate HDF files
 281 are created, reduced, and averaged for the geomagnetic eastward and northward com-
 282 ponents, and then the average of each component for each bin is used to create the vec-
 283 tor plots.

284 2.10 Spacecraft Inter-comparisons

285 Occasionally, two spacecraft fly through nearly the same region of space at nearly
 286 the same time. Previous studies (D. J. Knipp et al., 2014, 2015)) termed this event a 'mag-
 287 netic conjunction'. In contrast to a physical conjunction, which is a collision of two or-
 288 biting objects, a magnetic conjunction is a interval of time where two spacecraft were
 289 nearly co-located in magnetic coordinates ('on the same field line'). To find magnetic
 290 conjunctions using our data, we searched each bin Group from the aforementioned HDF5
 291 files for samples from different DMSP spacecraft which occurred within 90 seconds of
 292 each other. We then compared the bin-average Poynting flux measured by each space-
 293 craft to determine the degree of agreement. Using bin-average values allows us to com-
 294 pare primarily large scale (comparable to the bin size) structures, which are thought to
 295 vary more slowly than those with smaller scale size (e.g. D. J. Knipp et al. (2015)).

296 3 Results and Discussion

297 The data processing described in previous sections is an extension and improve-
 298 ment of that used in Rastätter et al. (2016) who reported a PF uncertainty of approx-
 299 imately $2.5mW/m^2$ using the good quality DMSP data. Recognizing that 'ground truth'
 300 for direct comparisons of PF could only come from estimates made by incoherent scat-
 301 ter radars, we try a different approach of inter-spacecraft comparison described below.

302 3.1 Spacecraft Inter-comparisons

303 Figure 5 shows comparisons (as scatterplots) of bin-average Poynting flux between
 304 each pair of DMSP spacecraft for more than 2000 such events. For all pairs of spacecraft,
 305 the Poynting flux measured is highly correlated (Spearman correlation (ρ) of .7 or higher).
 306 The trendline fits (calculated using a median-based robust regression) all have slopes close
 307 to 1, and large R^2 (coefficient of determination) values. This indicates all spacecraft mea-
 308 sure the same large-scale Poynting flux for the majority of conjunctions, to within some
 309 amount of scatter. The lower right element of the figure summarizes the three inter-comparisons
 310 as box-and-whisker plots for small ($< 5mW/m^2$) and large ($> 5mW/m^2$) values of Poynt-
 311 ing flux. The quantity plotted is percent difference in Poynting flux:

$$\Delta S_B = \frac{S_{B,1} - S_{B,2}}{\left(\frac{S_{B,1} + S_{B,2}}{2}\right)} * 100 \quad (9)$$

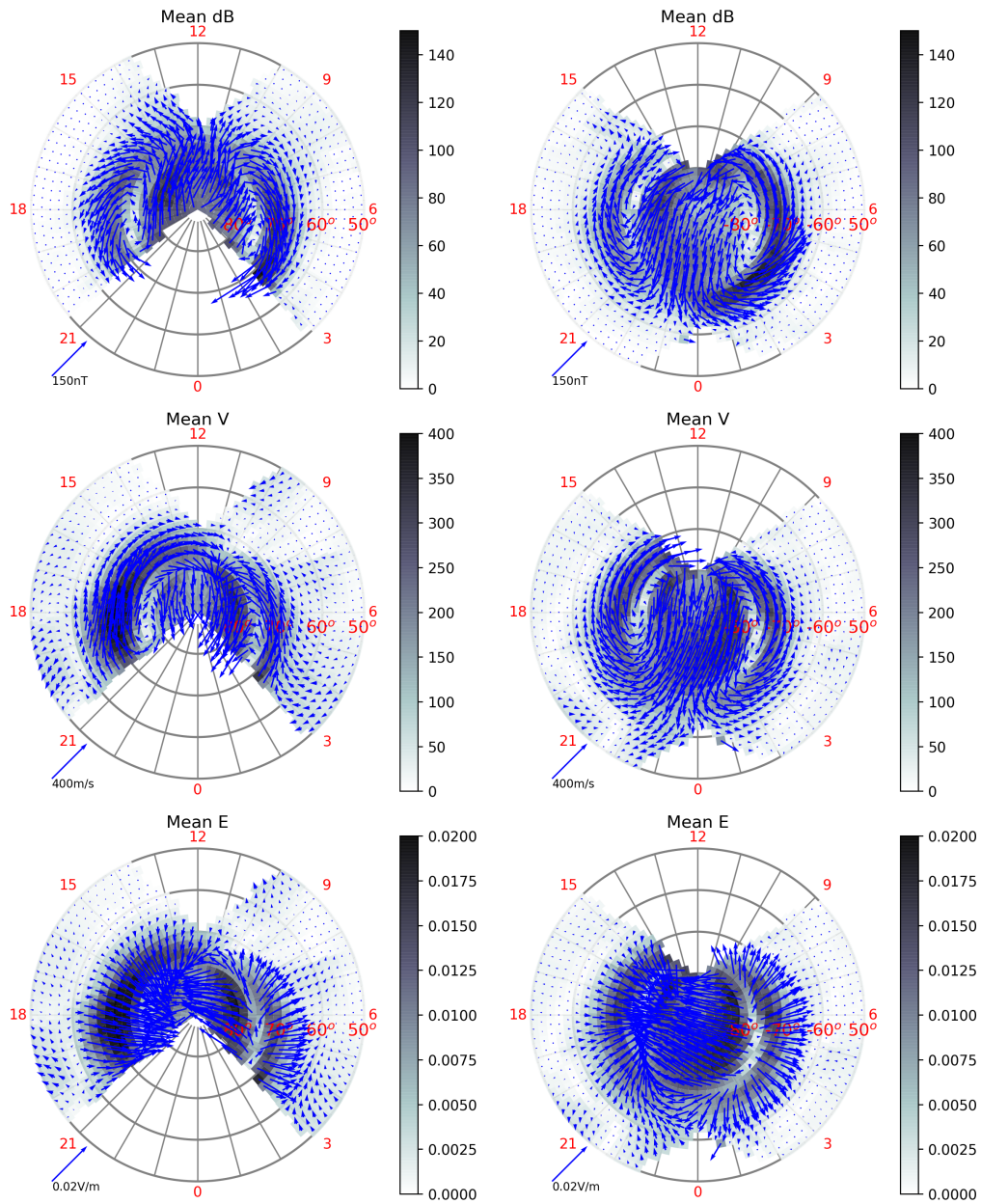


Figure 4. Electrodynamic vector parameters binned into equal area bins (each 2 degrees wide in latitude). The top row shows average magnetic perturbations; the middle row shows average ion drift vectors and the bottom row show average electric field vectors. Northern (Southern) hemisphere is on the left (right). Shading shows the vector magnitude.

Table 2. Integrated bin-average northern hemisphere Poynting flux (GW) (as show in figure 7)

Instrument	Total	MLT 8-16	MLT 16-24,0-8
IDM	22.8	6.8	15.9
IDM+RPA	31.9	11.3	20.6

312 The box-and-whisker plots show median as the black horizontal line, with the box edges
 313 at 25th and 75th percentile. The whiskers are median ± 1.5 *(inter-quartile range). The
 314 leftmost three boxes apply to conjunctions where the average Poynting flux (mean of the
 315 flux from the two spacecraft) was nearly negligible (less than $5mW/m^2$), while the right-
 316 most three boxes indicate conjunctions with non-negligible flux (average $> 5mW/m^2$).
 317 Concentrating on the larger Poynting flux values, slightly more systematic difference is
 318 seen for comparisons involving F15 (blue and red), with median percent difference of ap-
 319 proximately -30% (-28% for F15/F16, -31% for F15/F18). F15 carries the earlier gen-
 320 eration of ion drift instrumentation (SSIES2) which operates at a lower temporal cadence
 321 (.25 Hz) and produces less quality 1 data. Considering only spacecraft equipped with
 322 the newer SSIES3 drift instruments (F16 and F18) the median percent difference is -13%,
 323 indicating very good agreement.

324 3.2 Full Electric Field Versus Single Component Approximation

325 Many previous studies computing DMSP Poynting Flux have used only one com-
 326 ponent of the electric field (E_x in equation 5), derived from the across track (y direction)
 327 component of the ion drift velocity, and assuming all other velocity components are zero.
 328 The rationale for this is the along-track component of ion drift is measured by a differ-
 329 ent instrument (the RPA) which produces noisier velocity data and has more missing
 330 values. We are able to eliminate this approximation because we are using an improved
 331 version of the SSIES 3 data (see Table 1), and because our spatial bin-and-average re-
 332 duces the effect of the RPA noise. Note that we have used the full Poynting flux through-
 333 out this manuscript, except for the comparison in this section.

334 3.2.1 Effect on Inter-Spacecraft Poynting Flux Consistency

335 To illustrate the difference between single and full component Poynting flux, Fig-
 336 ure 6 shows the results of the magnetic conjunction analysis of Figure 5 using the sin-
 337 gular component approximation. For all 3 pairs of spacecraft, the line which approximates
 338 the average trend of the conjunctions does not have a slope close to 1, meaning on av-
 339 erage the Poynting flux measurements are not consistent. The correlations are also re-
 340 duced and the percent differences are larger with median values which are not as close
 341 to zero.

342 3.2.2 Effect on Spatial Poynting Flux Pattern

343 With an eye to the degradation of the conjunction analysis results using single com-
 344 ponent Poynting flux, figure 7 shows the resulting average spatial pattern of ion drift and
 345 Poynting flux. Unsurprisingly, there is overall less Poynting flux in the single component
 346 approximation, but importantly, there is significantly reduced Poynting flux in the noon
 347 high latitude (near-cusp) in the IDM-only view, even when accounting for the overall re-
 348 duction. Specifically, the integrated Poynting flux in the northern hemisphere day (8-
 349 16 MLT) sector drops from 11.3GW to 6.8GW (40%) between full and single compo-
 350 nent variants. In contrast the integrated flux from the remaining northern hemisphere
 351 bins drops only 20% (20.6GW to 15.9GW). This indicates that previous studies using
 352 single-component Poynting flux could underestimate the relative importance of this re-

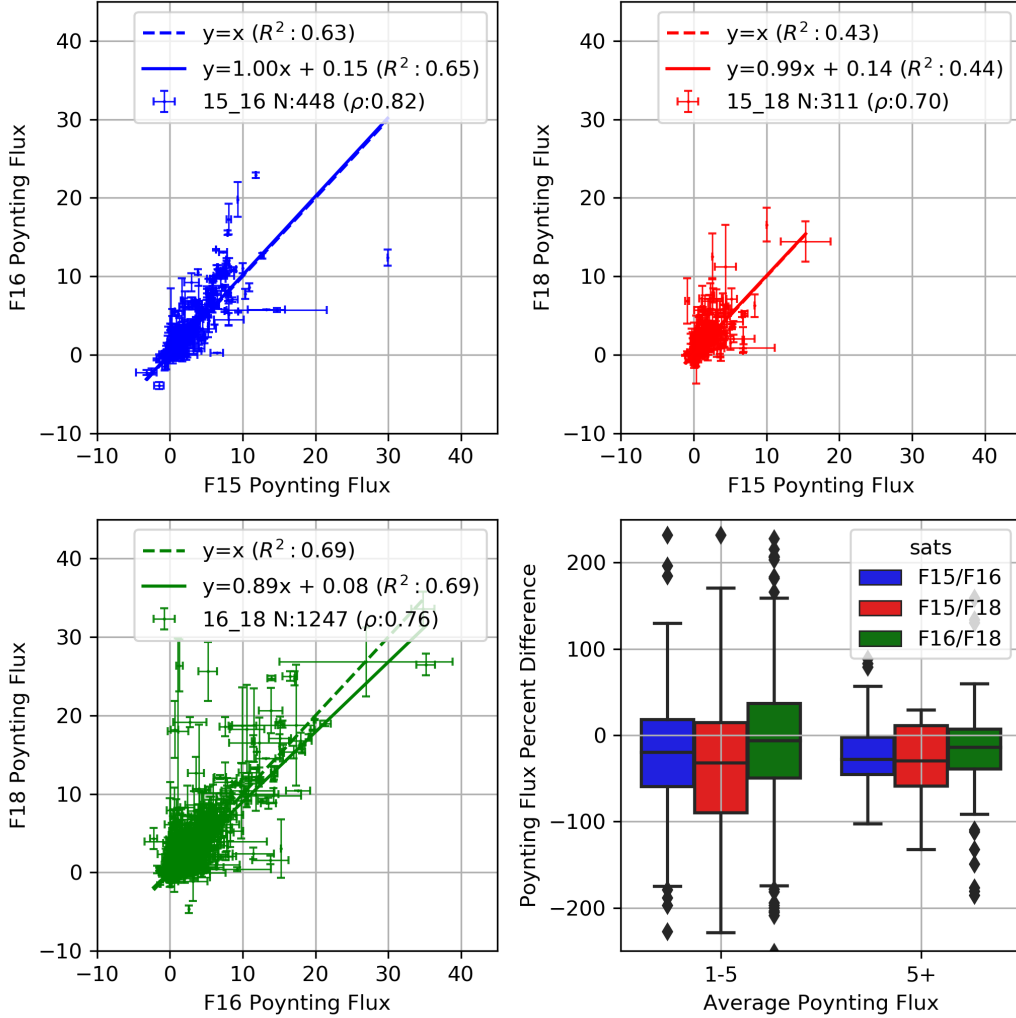


Figure 5. Poynting flux measured by each spacecraft involved in a magnetic conjunction. Top left, top right and bottom left panels show the bin-average Poynting flux for each magnetic conjunction between each pair of DMSP spacecraft, with error bars representing the bin standard deviation. The vertical error bars correspond to the spacecraft on the y-axis, and the horizontal error bars the spacecraft on the x-axis. Dashed lines represent the 'perfect match' line ($y = x$). Solid lines show the robust (Theil-Sen) linear fit to the data. Coefficient of determination (R^2) is shown for both lines. Lower right panel shows the percent difference of Poynting flux measured by each spacecraft pair during magnetic conjunctions.

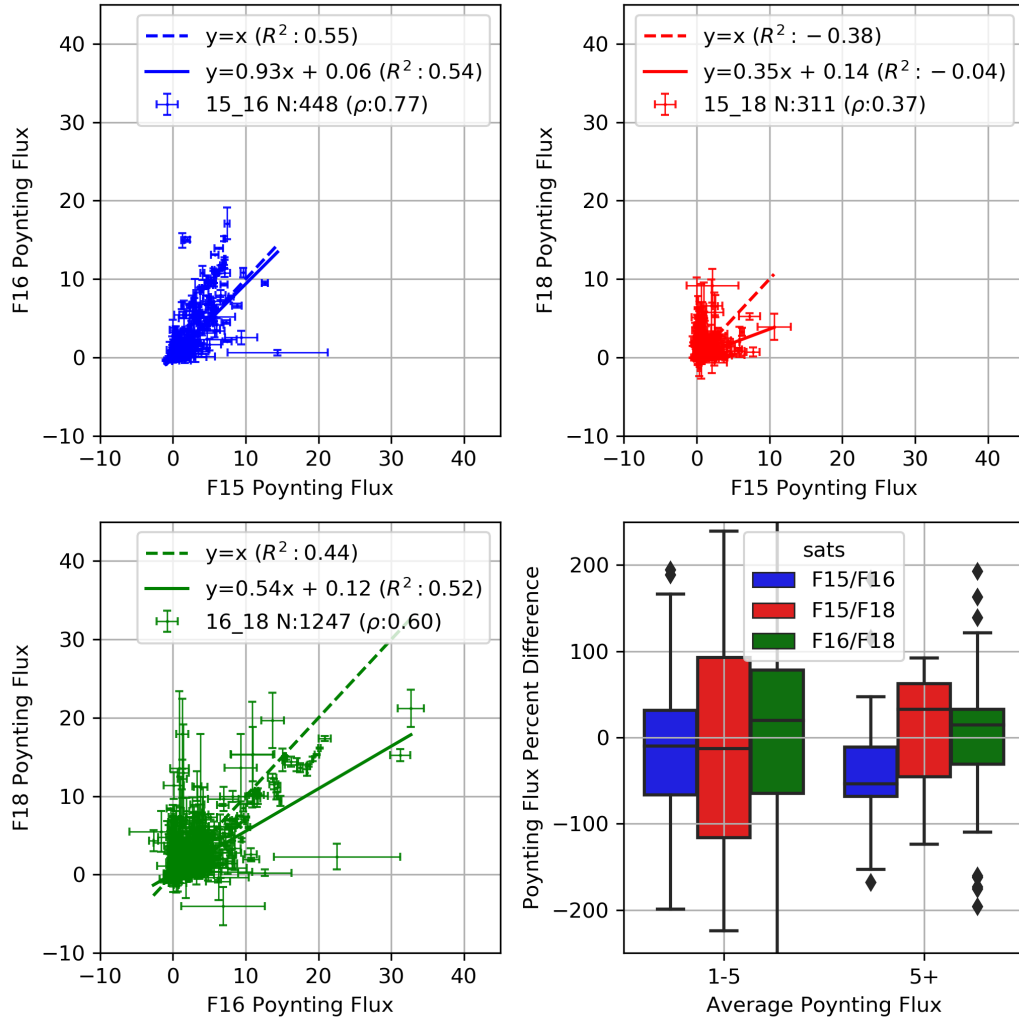


Figure 6. Poynting flux calculated using only one component of the electric field (derived from the cross track (IDM) velocity, with along-track and vertical velocities assumed 0) measured by each spacecraft involved in a magnetic conjunction (identical to Figure 5).

gion. Comparing the ion drift (the top 4 panels of Figure 7) suggests an explanation: the direction of ion flow in the near-cusp region is highly spatially variable, bending from sunward in the lower latitude to anti-sunward across the polar cap, and effect which is largely missed in the IDM-only picture. Moreover, the near-cusp flow is known to be particularly dynamic (for instance, the movement of the convection throat in response to changing IMF B_y). The spatial pattern of the average magnetic perturbations also bends in a similar manner (Figure 4) and we have verified it too is dynamic and sensitive to the direction of IMF B_y (not shown). Thus a missing electric field component is particularly problematic for resolving Poynting flux in this region.

4 Conclusions

We describe recent improvements to DMSP ion-convection data products that are incorporated into producing the 9 spacecraft-years of DMSP Poynting flux reported in D. Knipp et al. (2021). With the descriptions provided herein, we make the data processing routines and processed data available for general use. These improvements, which are applied to observations from three DMSP spacecraft, include an automated linear base-line correction for the ion drift measurements. These improvements along with the quality-flagging methods of Hairston and Coley (2019) support reproducible and consistent treatment of the full-vector electric field values, which along with the DMSP magnetic perturbations, are used in the Poynting flux estimates. Further, we describe a combined binning, averaging and storage routine for these data, which organizes the observations by location in magnetic coordinates, facilitating future analysis and discovery.

When applying the methods to full-component electric field values we find a 25% overall increase of globally integrated Poynting flux compared to Poynting flux determined from only the DMSP single-component electric field values. Inter-spacecraft comparisons clearly show that better Poynting flux agreement is achieved from the full-component electric field. The near cusp regions, where electric and magnetic field perturbations are constantly responding to the dynamic forcing of the solar wind and IMF component variations, are most affected by the use of the full-component values. Inter-spacecraft Poynting flux comparisons using this binned data showed good agreement, with median percent difference of 13% for comparisons between the latest-generation spacecraft (F16 and F18). We anticipate these new Poynting flux data products will be useful for future machine learning and empirical modeling efforts as well as model-data comparisons. Access points for the data and data processing routines are provided in section 5.

5 Open Research

5.1 Data

The data used in this paper (see table 1) were obtained from NASA Coordinated Data Analysis Web (CDAWeb) <https://spdf.gsfc.nasa.gov/pub/data/dmsp/> and from the CEDAR Madrigal database: <http://cedar.openmadrigal.org/list>. Access to DMSP F15 ion drift Madrigal data was accomplished using Pysat (R. Stoneback et al., 2021). The binned data products described herein are available on Zenodo (L. Kilcommons, 2022a).

5.2 Software

A general purpose Python software library implementing the equal area binning, storage, and retrieval scheme described herein has been published (L. Kilcommons, 2022b) and is developed at <https://github.com/lkilcommons/esabin>.

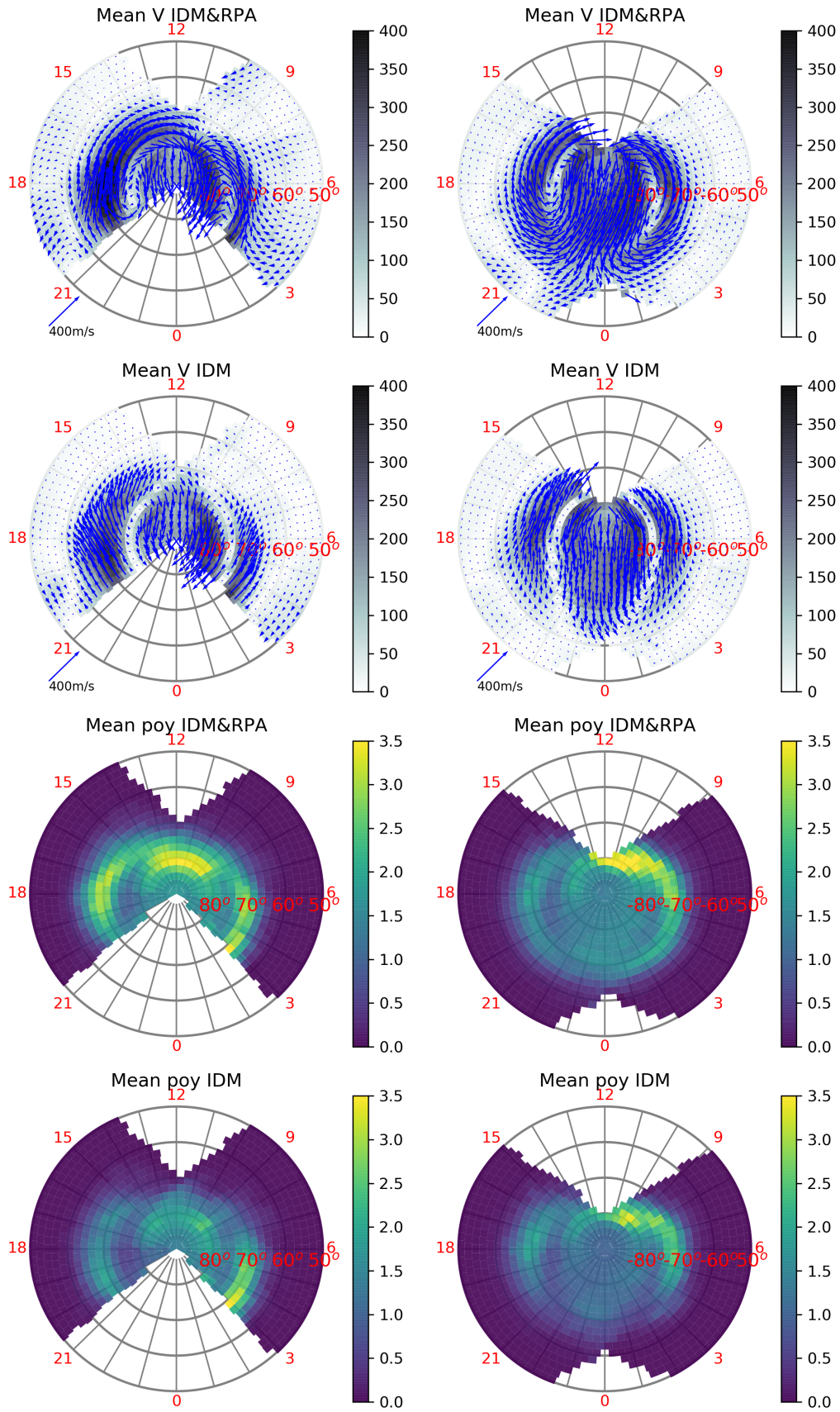


Figure 7. Spatial patterns of ion drift and Poynting Flux. The top row shows ion drift determined from along- and cross-track drifts. The second row shows only cross-track drift. The PF in the third row corresponds to the full drift component electric field. The bottom plots show PF calculated from only the cross-track (IDM) ion drift velocity). Northern hemisphere patterns are on the left and southern on the right.

Acknowledgments

LMK was partially supported by AFOSR Award No: FA9550-17-1-0258 and AFOSR MURI Award FA9550-16-1-0364. DJK was partially supported by AFOSR Award No: FA9550-17-1-0258 and by NASA Award 80NSSC20K1784. MH and RC were supported by NASA Grant 80NSSC20K1071.

References

- Cole, K. D. (1966). Magnetic storms and associated phenomena. *Space Sci Rev*, 5, 699-770. doi: <https://doi.org/10.1007/BF00173103>
- Cosgrove, R. B., Bahcivan, H., Chen, S., Strangeway, R. J., Ortega, J., Alhassan, M., ... Cahill, N. (2014). Empirical model of poynting flux derived from fast data and a cusp signature. *Journal of Geophysical Research: Space Physics*, 119(1), 411-430. Retrieved from <https://agupubs.onlinelibrary.wiley.com/doi/abs/10.1002/2013JA019105> doi: <https://doi.org/10.1002/2013JA019105>
- Dessler, A. J. (1959). Upper atmosphere density variations due to hydromagnetic heating. *Nature*, 184, 261-262. doi: <https://doi.org/10.1038/184261b0>
- Emmert, J. T., Richmond, A. D., & Drob, D. P. (2010). A computationally compact representation of magnetic-apex and quasi-dipole coordinates with smooth base vectors. *Journal of Geophysical Research: Space Physics*, 115(A8). Retrieved from <https://agupubs.onlinelibrary.wiley.com/doi/abs/10.1029/2010JA015326> doi: <https://doi.org/10.1029/2010JA015326>
- Gary, J. B., Heelis, R. A., & Thayer, J. P. (1995). Summary of field-aligned poynting flux observations from de 2. *Geophysical Research Letters*, 22(14), 1861-1864. Retrieved from <https://agupubs.onlinelibrary.wiley.com/doi/abs/10.1029/95GL00570> doi: <https://doi.org/10.1029/95GL00570>
- Hairston, M., & Coley, W. R. (2019, September). *A Short Introduction to the DMSP SSIES-3 Quality Flags and How to Use Them*. Zenodo. Retrieved from <https://doi.org/10.5281/zenodo.4776161> doi: 10.5281/zenodo.4776161
- Huang, C. Y., Huang, Y., Su, Y.-J., Hairston, M. R., & Sotirelis, T. (2017). Dmsp observations of high latitude poynting flux during magnetic storms. *Journal of Atmospheric and Solar-Terrestrial Physics*, 164, 294-307. Retrieved from <https://www.sciencedirect.com/science/article/pii/S1364682617305151> doi: <https://doi.org/10.1016/j.jastp.2017.09.005>
- Jacchia, G., Luigi. (1959a). Two atmospheric effects in the orbital acceleration of artificial satellites. *Nature*, 183, 526-527. Retrieved from <https://doi.org/10.1038/183526a0> doi: 10.1038/183526a0
- Jacchia, G., Luigi. (1959b). Corpuscular radiation and the acceleration of artificial satellites. *Nature*, 183, 1662-1663. Retrieved from <https://doi.org/10.1038/1831662a0> doi: 10.1038/1831662a0
- Kaeppeler, S. R., Knipp, D. J., Verkhoglyadova, O. P., Kilcommons, L. M., & Zhan, W. (2022). Chapter 5 - electromagnetic energy input and dissipation. In Y. Nishimura, O. Verkhoglyadova, Y. Deng, & S.-R. Zhang (Eds.), *Cross-scale coupling and energy transfer in the magnetosphere-ionosphere-thermosphere system* (p. 301-355). Elsevier. Retrieved from <https://www.sciencedirect.com/science/article/pii/B9780128213667000068> doi: <https://doi.org/10.1016/B978-0-12-821366-7.00006-8>
- Kilcommons, L. (2022a, January). *DMSP F15/F16/F18 2011-2014 Binned Poynting Flux Data* [dataset]. Zenodo. Retrieved from <https://doi.org/10.5281/zenodo.5829535> doi: 10.5281/zenodo.5829535
- Kilcommons, L. (2022b, January). *lkilcommons/esabin: v0.2.2* [software]. Zenodo. Retrieved from <https://doi.org/10.5281/zenodo.5842038> doi: 10.5281/zenodo.5842038
- Kilcommons, L. M., Redmon, R. J., & Knipp, D. J. (2017). A new dmsp mag-

- 450 netometer and auroral boundary data set and estimates of field-aligned
 451 currents in dynamic auroral boundary coordinates. *Journal of Geophysi-*
 452 *cal Research: Space Physics*, 122(8), 9068-9079. Retrieved from [https://](https://agupubs.onlinelibrary.wiley.com/doi/abs/10.1002/2016JA023342)
 453 agupubs.onlinelibrary.wiley.com/doi/abs/10.1002/2016JA023342 doi:
 454 10.1002/2016JA023342
- 455 Knipp, D., Eriksson, S., Kilcommons, L., Crowley, G., Lei, J., Hairston, M., &
 456 Drake, K. (2011). Extreme poynting flux in the dayside thermosphere:
 457 Examples and statistics. *Geophysical Research Letters*, 38(16). Retrieved
 458 from [https://agupubs.onlinelibrary.wiley.com/doi/abs/10.1029/](https://agupubs.onlinelibrary.wiley.com/doi/abs/10.1029/2011GL048302)
 459 [2011GL048302](https://agupubs.onlinelibrary.wiley.com/doi/abs/10.1029/2011GL048302) doi: <https://doi.org/10.1029/2011GL048302>
- 460 Knipp, D., Kilcommons, L., Hairston, M., & Coley, W. R. (2021). Hemispheric
 461 asymmetries in poynting flux derived from dmSP spacecraft. *Geophysi-*
 462 *cal Research Letters*, 48(17), e2021GL094781. Retrieved from [https://](https://agupubs.onlinelibrary.wiley.com/doi/abs/10.1029/2021GL094781)
 463 agupubs.onlinelibrary.wiley.com/doi/abs/10.1029/2021GL094781
 464 (e2021GL094781 2021GL094781) doi: <https://doi.org/10.1029/2021GL094781>
- 465 Knipp, D. J., Kilcommons, L. M., Gjerloev, J., Redmon, R. J., Slavin, J., & Le,
 466 G. (2015, April). A large-scale view of Space Technology 5 magnetometer
 467 response to solar wind drivers. *Earth and Space Science*, 2(4), 2014EA000057.
 468 Retrieved 2016-08-10, from [http://onlinelibrary.wiley.com/doi/10.1002/](http://onlinelibrary.wiley.com/doi/10.1002/2014EA000057/abstract)
 469 [2014EA000057/abstract](http://onlinelibrary.wiley.com/doi/10.1002/2014EA000057/abstract) doi: 10.1002/2014EA000057
- 470 Knipp, D. J., Matsuo, T., Kilcommons, L., Richmond, A., Anderson, B., Korth, H.,
 471 ... Parrish, N. (2014). Comparison of magnetic perturbation data from leo
 472 satellite constellations: Statistics of dmSP and ampere. *Space Weather*, 12(1),
 473 2-23. Retrieved from [https://agupubs.onlinelibrary.wiley.com/doi/abs/](https://agupubs.onlinelibrary.wiley.com/doi/abs/10.1002/2013SW000987)
 474 [10.1002/2013SW000987](https://agupubs.onlinelibrary.wiley.com/doi/abs/10.1002/2013SW000987) doi: <https://doi.org/10.1002/2013SW000987>
- 475 Laundal, K. M., & Richmond, A. D. (2017, March). Magnetic Coordinate Systems.
 476 *Space Science Reviews*, 206(1), 27–59. Retrieved 2022-01-11, from [https://](https://doi.org/10.1007/s11214-016-0275-y)
 477 doi.org/10.1007/s11214-016-0275-y doi: 10.1007/s11214-016-0275-y
- 478 Mosier, S. R., & Gurnett, D. A. (1969). Vlf measurements of the poynting flux
 479 along the geomagnetic field with the injun 5 satellite. *Journal of Geophys-*
 480 *ical Research (1896-1977)*, 74(24), 5675-5687. Retrieved from [https://](https://agupubs.onlinelibrary.wiley.com/doi/abs/10.1029/JA074i024p05675)
 481 agupubs.onlinelibrary.wiley.com/doi/abs/10.1029/JA074i024p05675
 482 doi: <https://doi.org/10.1029/JA074i024p05675>
- 483 Olsson, A., Janhunen, P., Karlsson, T., Ivchenko, N., & Blomberg, L. G. (2004).
 484 Statistics of joule heating in the auroral zone and polar cap using astrid-2
 485 satellite poynting flux. *Annales Geophysicae*, 22(12), 4133–4142. Retrieved
 486 from <https://angeo.copernicus.org/articles/22/4133/2004/> doi:
 487 10.5194/angeo-22-4133-2004
- 488 Pakhotin, I., . Mann, I. R., Xie, K., Burchill, J. K., & Knudsen, D. J. (2021).
 489 Northern preference for terrestrial electromagnetic energy input from space
 490 weather. *Nature Communications*, 12(1). doi: [https://doi.org/10.1038/](https://doi.org/10.1038/s41467-020-20450-3)
 491 [s41467-020-20450-3](https://doi.org/10.1038/s41467-020-20450-3)
- 492 Rastätter, L., Shim, J. S., Kuznetsova, M. M., Kilcommons, L. M., Knipp, D. J.,
 493 Codrescu, M., ... Welling, D. (2016, February). GEM-CEDAR challenge:
 494 Poynting flux at DMSP and modeled Joule heat. *Space Weather*, 14(2), 113-
 495 135. doi: 10.1002/2015SW001238
- 496 Rich, F. J., Bono, J. M., Burke, W. J., & Gentile, L. C. (2007, May). A space-based
 497 proxy for the Dst index. *Journal of Geophysical Research (Space Physics)*,
 498 112(A5), A05211. doi: 10.1029/2005JA011586
- 499 Stoneback, R., Klenzing, J., Burrell, A. G., Pembroke, A., Spence, C., Depew,
 500 M., ... Leite, S. (2021, July). *pysat/pysat: v3.0.1* [software]. Zen-
 501 odo. Retrieved from <https://doi.org/10.5281/zenodo.5142690> doi:
 502 10.5281/zenodo.5142690
- 503 Stoneback, R. A., Burrell, A. G., Klenzing, J., & Depew, M. D. (2018). PYSAT:
 504 Python Satellite Data Analysis Toolkit. *Journal of Geophysical Research:*

- 505 *Space Physics*, 123(6), 5271–5283. doi: 10.1029/2018JA025297
506 van der Meeren, C., Laundal, K. M., Burrell, A. G., Starr, G., Reimer, A. S., &
507 Morschhauser, A. (2021, March). *aburrell/apexpy: Apexpy version 1.1.0* [soft-
508 ware]. Zenodo. Retrieved from <https://doi.org/10.5281/zenodo.4585641>
509 doi: 10.5281/zenodo.4585641
- 510 Weimer, D. R. (2005). Improved ionospheric electrodynamic models and appli-
511 cation to calculating joule heating rates. *Journal of Geophysical Research:*
512 *Space Physics*, 110(A5). Retrieved from [https://agupubs.onlinelibrary](https://agupubs.onlinelibrary.wiley.com/doi/abs/10.1029/2004JA010884)
513 [.wiley.com/doi/abs/10.1029/2004JA010884](https://agupubs.onlinelibrary.wiley.com/doi/abs/10.1029/2004JA010884) doi: [https://doi.org/10.1029/](https://doi.org/10.1029/2004JA010884)
514 [2004JA010884](https://doi.org/10.1029/2004JA010884)